



Published in final edited form as:

Oncogene. 2023 July ; 42(30): 2347–2359. doi:10.1038/s41388-023-02756-w.

Critical role of antioxidant programs in enzalutamide-resistant prostate cancer

Eliot B. Blatt¹, Karla Parra¹, Antje Neeb², Lorenzo Buroni², Denisa Bogdan², Wei Yuan², Yunpeng Gao³, Collin Gilbreath¹, Alec Paschalis², Suzanne Carreira², Ralph J. DeBerardinis^{4,5}, Ram S. Mani^{1,3}, Johann S. de Bono^{2,6}, Ganesh V. Raj^{1,7,8,*}

¹Department of Urology, University of Texas Southwestern Medical Center at Dallas, Dallas, TX, 75390, USA

²The Institute of Cancer Research, London, UK

³Department of Pathology, University of Texas Southwestern Medical Center at Dallas, Dallas, TX, 75390, USA

⁴Children's Medical Center Research Institute, University of Texas Southwestern Medical Center at Dallas, 5323 Harry Hines Boulevard, Dallas, TX, 75390, USA

⁵Howard Hughes Medical Institute, University of Texas Southwestern Medical Center at Dallas, 5323 Harry Hines Boulevard, Dallas, TX 75390, USA

⁶Institute of Cancer Research and the Royal Marsden NHS Foundation Trust, London, UK

⁷Department of Pharmacology, University of Texas Southwestern Medical Center at Dallas, Dallas, TX, 75390

⁸Harold C. Simmons Comprehensive Cancer Center, University of Texas Southwestern Medical Center at Dallas, Dallas, TX, 75390, USA

Abstract

*Corresponding Author: Ganesh.Raj@utsouthwestern.edu.
Author Contributions

Experiments were conceptualized, performed, and analyzed by EBB. EBB also responsible for methodology, funding acquisition, and writing the original and editing further manuscript drafts. Funding was acquired, experiments performed, and editing manuscript drafts by KP. Experiments performed and manuscript drafts edited by AN and LB. Formal analysis performed and manuscript drafts edited by YG, DB, and WY. Manuscript drafts edited by AP and SC. Experiments performed and manuscript drafts edited by CG. Methodology, supervision, and manuscript drafts edited by RJD. Supervision and manuscript drafts edited by RSM and JSdB. Funding acquisition, methodology, supervision, and manuscript drafts edited by GVR.

Conflict of interest disclosure statement: GVR serves or has served in an advisory role to Bayer, Johnson and Johnson, Myovant, EтираRx, Amgen, Pfizer and Astellas. He has or has had grant support from Bayer, EтираRx and Johnson and Johnson. RJD is a founder and advisor for Atavistik Bioscience, and a scientific advisor for Agios Pharmaceuticals, Nirology Therapeutics, Droia Ventures, and Vida Ventures. JSdB has served on advisory boards and received fees from Amgen, Astra Zeneca, Astellas, Bayer, Bioexcel Therapeutics, Boehringer Ingelheim, Cellcentric, Daiichi, Eisai, Genentech/Roche, Genmab, GSK, Harpoon, ImCheck Therapeutics, Janssen, Merck Serono, Merck Sharp & Dohme, Menarini/Silicon Biosystems, Orion, Pfizer, Qiagen, Sanofi Aventis, Sierra Oncology, Taiho, Terumo, and Vertex Pharmaceuticals; is an employee of the Institute of Cancer Research (ICR), which have received funding or other support for his research work from AZ, Astellas, Bayer, Cellcentric, Daiichi, Genentech, Genmab, GSK, Janssen, Merck Serono, MSD, Menarini/Silicon Biosystems, Orion, Sanofi Aventis, Sierra Oncology, Taiho, Pfizer, and Vertex, and which has a commercial interest in abiraterone, PARP inhibition in DNA repair defective cancers, and PI3K/AKT pathway inhibitors (no personal income); was named as an inventor, with no financial interest for patent 8 822 438, submitted by Janssen that covers the use of abiraterone acetate with corticosteroids; has been the CI/PI of many industry-sponsored clinical trials; and is a National Institute for Health Research (NIHR) Senior Investigator. AN, LB, DB, WY, AP, SC, and JSdB are employees of the Institute of Cancer Research (ICR), which has commercial interest in abiraterone. No other authors have any potential conflicts of interest to disclose.

Therapy resistance to second generation androgen receptor (AR) antagonists, such as enzalutamide, is common in patients with advanced prostate cancer (PCa). To understand the metabolic alterations involved in enzalutamide resistance, we performed metabolomic and transcriptomic analyses of enzalutamide-sensitive and -resistant PCa cells, xenografts, patient-derived organoids, patient-derived explants, and tumors. We noted dramatically higher basal and inducible levels of reactive oxygen species (ROS) in enzalutamide-resistant PCa and castration-resistant PCa (CRPC), in comparison to enzalutamide-sensitive PCa cells or primary therapy-naïve tumors respectively. Unbiased metabolomic evaluation identified that glutamine metabolism was consistently upregulated in enzalutamide-resistant PCa cells and CRPC tumors. Stable isotope tracing studies suggest that this enhanced glutamine metabolism drives an antioxidant program that allows these cells to tolerate higher basal levels of ROS. Inhibition of glutamine metabolism with either a small-molecule glutaminase inhibitor or genetic knockout of glutaminase enhanced ROS levels, and blocked the growth of enzalutamide-resistant PCa. The critical role of compensatory antioxidant pathways in maintaining enzalutamide-resistant PCa cells was validated by targeting another antioxidant program driver, ferredoxin 1. Taken together, our data identify a metabolic need to maintain antioxidant programs and a potentially targetable metabolic vulnerability in enzalutamide-resistant PCa.

Introduction

Prostate cancer (PCa) is primarily driven by the androgen receptor (AR) and grows in response to androgens [1-3]. Patients with metastatic PCa are treated with medical or surgical castration to remove androgens and block AR signaling and tumor growth. Despite castrate levels of circulating androgens, castration-resistant prostate cancer (CRPC) emerges and is still primarily driven by the AR [4-11]. The development of second-generation AR antagonists, such as enzalutamide, darolutamide, and apalutamide, enabled more robust AR antagonism and have been shown to improve overall survival across multiple disease stages, including CRPC [12-18]. However, these antiandrogens are rarely curative and therapy resistance is common. Like other cancers, enzalutamide-resistant PCa is characterized by rapid cell growth and proliferation, which requires increased nucleotides for the synthesis of DNA/RNA, lipids for cell membranes, and amino acids for protein translation. Anticancer therapies target these metabolic processes and can cause cancer cell death [19-21]. Since the metabolic mechanisms underlying enzalutamide resistance are not well-characterized, we performed metabolic profiling of enzalutamide-sensitive (EnzS) and enzalutamide-resistant (EnzR) PCa cell lines, xenografts, patient-derived explants, patient-derived organoids, and patient tumors. Overall, our data show that EnzR-PCa have both a higher basal and inducible level of reactive oxygen species (ROS), compared to EnzS-PCa. We demonstrate that antioxidant programs are critical for the survival of EnzR-PCa, and that targeting antioxidant programs in EnzR-PCa may be a viable therapeutic strategy.

Materials and Methods

Cell culture

EnzS and EnzR LNCaP, C4-2B, and CWR-R1 cell lines were passage-matched and cultured in RPMI-1640 supplemented with 10% FBS and 1% penicillin-streptomycin at 37C, 5%

CO₂. EnzS and EnzR LAPC-4 were passage-matched and cultured in Isocove's Modified Dulbecco's Medium supplemented with 10% FBS and 1% penicillin-streptomycin. EnzR cell lines were maintained in either 10 or 20 uM enzalutamide (LNCaP (UIC) from the Vander Griend lab [22], LNCaP (VCH) from the Zoubeidi lab [23], CWR-R1 and LAPC-4 from the Vander Griend lab [22] in 10 uM and LNCaP (UTSW) from the Hsieh lab and C4-2B from the Gao lab via the Hsieh lab [24] in 20 uM enzalutamide). All cell lines were authenticated by STR profiling and tested negative for mycoplasma recently.

Organoid culture

Patient-derived organoids were cultured using a method adapted from previously published methods [25], with minor alterations. Briefly, patient-derived xenograft (PDX) tumors were harvested in PDX harvesting solution (adMEM/F12 containing 10 μ M ROCK inhibitor Y27632 (Selleck Chemicals), penicillin/streptomycin, 10 mM Hepes and GlutaMAX 100x diluted (all purchased from Thermofisher), cut into small pieces (< 5 mm²), and single cell suspensions were generated by mechanical separation (40 μ m Corning cell strainer, Sigma Aldrich). Pellets were washed once with ice-cold PBS/10 μ M Y27632, and red blood cells were removed using red blood cell lysis buffer (0.8% NH₄Cl in 0.1 mM EDTA in water, buffered with KHCO₃ to pH of 7.2 - 7.6, incubated 1 min on ice) followed by another wash with ice cold PBS/Y27632. Single cell suspensions were either frozen for later use in BioCat Bambanker™ freezing medium (Fisher Scientific) supplemented with 10 μ M Y27632, or directly resuspended in ice-cold organoid growth medium (as previously published [25], with the following alterations: the p38 inhibitor SB202190 was replaced by the addition of 5 nM of NRG1 and subsequently diluted in one volume of phenol red-free, growth factor reduced, Corning Matrigel™ (Fisher Scientific)). Organoid domes (5-50 μ l) were plated, as previously described [25] and topped up with warm medium after solidification. Cultures were observed over 3-7 days until visible organoid formation was established. Cell line organoids were cultured as follows: cells were detached from culture flask using TrypLE™ Express Enzyme (1X), phenol red (Fisher Scientific). Single cell suspensions were directly resuspended in ice-cold RPMI 1640 Medium, GlutaMAX™ Supplement (Fisher Scientific) and subsequently diluted in one volume of phenol red-free, growth factor reduced, Corning Matrigel™ (Fisher Scientific). Organoid domes (5-50 μ l) were plated, as previously described [25], and topped up with warm medium after solidification. Cultures were observed over 3-7 days until visible organoid formation was established.

ChIP-Seq and ChiA-PET analyses

Integrative genomics viewer (IGV) was used to overlay AR ChIP-seq, H3K27ac ChIP-seq, and RNA polymerase II CHIA-PET in LNCaP cells. AR ChIP data was obtained from GEO ID: GSM2480800 and GEO ID: GSM2480801, as described in [26] and GEO ID: GSM3424005, as described in [27]. H3K27ac ChIP was obtained from GEO ID: GSM1902615, as described in [28]. RNA polymerase II CHIA-PET was obtained from GEO ID: GSM3423998, as described in [27].

Steady-state metabolomics

1-3 x 10⁶ adherent cells were plated. To collect metabolites, plates were washed with cold saline, 1 mL of 80% MeOH or 80% MeOH + 0.1% formic acid (cooled to -80C) was

added to the plate on dry ice, and stored at -80°C for 20-30 minutes. Cells were scraped into tubes on dry ice and subjected to three freeze-thaw cycles with liquid nitrogen and 37°C water bath. Tubes were vortexed for one minute, centrifuged for 15 minutes at 20, 200 x g, and the metabolite-containing supernatant was transferred to a new tube and was dried with SpeedVac using no heat to a pellet. Patient and mice tumors (ranging from 10-900 mg) were flash-frozen in liquid nitrogen, cut into small pieces on dry ice, and homogenized in a tissue homogenizer in 1 mL 80% MeOH + 0.1% formic acid with 7-8 cycles of: 2 x 6200 rpm for 20 seconds and 30 second pause (cooled to dry ice between cycles) and vortexed for 20 seconds. 200 μL tissue-containing mixture was diluted to 1 mL in 80% methanol (MeOH) + 0.1% formic acid, vortexed for 1 minute, centrifuged for 15 minutes at 20,200 x g, and the metabolite-containing supernatant was transferred to a new tube and dried with SpeedVac using no heat to a pellet. Organoids underwent the same protocol as patient and mice tumors, except the matrigel dome was scraped into tubes, was homogenized by ultrasonicator on ice, and were not diluted 1:5 in MeOH, prior to centrifugation. Samples were run on the Agilent 6550 iFunnel LC/quadrupole-time of flight mass spectrometer for unbiased metabolite profiling and the AB SCIEX QTRAP 5500 LC/triple quadruple mass spectrometer for targeted metabolomics. Heatmaps were generated with software from <https://software.broadinstitute.org/morpheus/> and <http://www.heatmapper.ca/>.

Stable isotope tracing

$1-3 \times 10^6$ adherent cells were plated. 24 hrs after plating, cells were washed with PBS, and replaced with RPMI-1640 without glutamine, substituted with 0.3 g/L (2 mM) [$\text{U-}^{13}\text{C}$] glutamine, 5% dialyzed FBS, and 1% penicillin-streptomycin. Cells were harvested at 1, 3, 6, 12, and 24 hrs, according to the protocol used for steady-state metabolomics in 80% MeOH. Samples were run on the AB SCIEX QTRAP 5500 LC/triple quadruple mass spectrometer. Samples were normalized to total ion content and individual metabolite values were further normalized relative to glutamine.

Transcriptomic analysis

Integrated pathway analysis of metabolomic and transcriptomic data performed using joint pathway analysis software from <https://www.metaboanalyst.ca/> with significantly altered genes from [29] and [30]. Heatmaps of AR-regulated glutamine and antioxidant genes were generated with software from <https://software.broadinstitute.org/morpheus/> and display significantly altered genes from [29, 31, 32]. Patient tumor transcriptome analysis: RNA-seq data was obtained from SU2C mCRPC study ($n = 159$). RNA-seq data for the RMH cohort ($n = 95$) was obtained as previously described [33]. Both mCRPC cohorts were analyzed as previous described [34, 35]. TCGA ($n = 494$) data are available under Broad Institute GDAC TCGA Analysis Pipeline License. Pathway analysis was performed using the Gene Set Enrichment Analysis (GSEA) Pre-Ranked algorithm from GSEA software (v4.1.0).

ROS Assays

To measure ROS, cells were incubated with 5 μM CM- H_2DCFDA in the dark for 30 minutes at 37°C . Cells were washed with pre-warmed HBSS before and after the ROS indicator was added. For hydrogen peroxide assays, media was replaced with media containing vehicle or 1 mM hydrogen peroxide, and cells were treated for 30 minutes, prior to imaging. For

fluorescence microscopy, 40x images were taken using the Spinning disk confocal Nikon CSU-W1 with SoRa using the GFP channel and individual cells were quantified by median fluorescence intensity (MFI) using ImageJ. For flow cytometry, cells were harvested in trypsin and neutralized with media, pelleted, washed with cold PBS, resuspended in 500 uL Annexin V binding buffer, strained with 35 uM cell strainers, and kept on ice, prior to measuring by flow cytometry. The LSRFortessa SCC or LSR Fortessa SORP analyzers were used to measure ROS. Cells were gated by FSC and SSC to select cells and remove doublets, and gated by Annexin V and PI staining to select live cells. ROS was measured using the FITC channel, and FITC+ cells were gated, based on unstained controls, and quantified by median fluorescence intensity (MFI).

GSH Assays

To measure GSH, cells were harvested in trypsin neutralized with media, pelleted, and incubated in 10 uM ThiolTracker Violet in the dark for 30 minutes at 37C (cells resuspended prior to incubation). Cells were washed with pre-warmed PBS with Ca^{2+} and Mg^{2+} before and after pelleting. After incubation in ThiolTracker Violet, cells were pelleted, washed and resuspended in 500 uL cold PBS with Ca^{2+} and Mg^{2+} , prior to being strained with 35 uM cell strainers and kept on ice, prior to measuring by flow cytometry. The LSRFortessa SCC or LSR Fortessa SORP analyzers were used to measure GSH. Cells were gated by FSC and SSC to select cells and remove doublets, gated by Annexin V and PI staining to select live cells. GSH was measured using the BV510 channel, and BV510+ cells were gated, based on unstained controls, and quantified using median fluorescence intensity (MFI).

Annexin V and PI Staining

For apoptosis assays, media was collected prior to cells being trypsinized. After cells were strained for ROS and GSH assays, 100 uL of cell-containing mixture in Annexin V binding buffer was transferred to a new flow tube, 5 uL Alexa Fluor 647 Annexin V antibody and 1 uL 100 ug/mL propidium iodide was added, vortexed briefly, and incubated for 15 minutes in the dark at room temperature. 400 uL Annexin V binding buffer was added and cells were kept on ice, prior to measuring by flow cytometry. The LSRFortessa SCC or LSR Fortessa SORP analyzers were used to measure Annexin V and PI. Cells were gated by FSC and SSC to select cells and remove doublets, and gated by Annexin V and PI staining to select live cells, based on unstained controls. PI was measured using the PI or PE-Alexa Fluor 610 channel, Annexin V was measured using the Alexa Fluor 647 channel, and the percentage of cells in each quadrant was used to determine apoptotic cells (Q3 for early apoptosis and Q2 for late apoptosis).

Lipid Peroxide Assays

To measure lipid peroxides, cells were incubated in the Image-iT Lipid Peroxidation Sensor in the dark for 30 minutes at 37C. Cells were washed with pre-warmed PBS, harvested in trypsin neutralized with media, pelleted, washed with cold PBS, strained in 35 uM cell strainers, and kept on ice prior to measuring by flow cytometry. The LSRFortessa SCC or LSR Fortessa SORP analyzers were used to measure lipid peroxides. Cells were gated by FSC and SSC to select cells and remove doublets. Lipid peroxides were measured using FITC and Texas Red channels and gated, based on unstained controls. The ratio of

Texas Red to FITC was used to show reduced:oxidized lipids and quantified using median fluorescence intensity (MFI).

MitoTracker Assays

To measure mitochondrial content, cells were incubated in MitoTracker Green for Flow Cytometry indicator in suspension in the dark for 30 minutes at 37C. Cells were washed with cold PBS, pelleted, and resuspended in 500 uL Annexin V binding buffer, strained with 35 uM cell strainers, and kept on ice prior to analysis. The LSRFortessa SCC or LSR Fortessa SORP analyzers were used to measure MitoTracker. Cells were gated by FSC and SSC to select cells and remove doublets, gated by Annexin V and PI staining to select live cells. Mitochondrial content was measured using the FITC channel, and FITC+ cells were gated, based on unstained controls, and quantified using median fluorescence intensity (MFI).

Tissue Collagenase Digestion

Tissue was cut into 1 mm³ pieces, washed in cold PBS, pelleted, washed in cold HBSS, and incubated on rotation in 35 mL HBSS, 5 mg/mL type I collagenase, 1x penicillin-streptomycin, 10 uM DHT, 10 uM ROCK inhibitor Y-27632, and DNase I at 37C for approximately two hours. Tissue-collagenase solution was then washed with cold PBS, pelleted, re-suspended in 5 mL TryLE Express and incubated at 37C for five minutes. Trypsin was neutralized with Dulbecco's Modified Eagle Medium-high glucose supplemented with 10% FBS and 1% penicillin-streptomycin, and cells were pelleted and resuspended in 1 mL DMEM. Cells were then strained with a 40 uM cell strainer and prepared for ROS assay, following the ROS assay protocol for flow cytometry. For hydrogen peroxide assays, cells were treated in suspension with media containing vehicle or 1 mM hydrogen peroxide for 15 minutes, prior to analysis.

Cell viability assays

1.5-3.0 x 10³ cells were plated in 48-well plates for 6-8 days and cell viability was assessed by hoescht staining. For hoescht staining, media was aspirated, 250 uL ultra-pure distilled water was added to each well, and the plates were frozen at -20C overnight. The following day, the wells were thawed, and 500 uL bisbenzimidazole Hoescht 33342 (10 ug/mL) in 1 mM EDTA (pH 8.0), 2 M NaCl, 10 mM Tris HCl (pH 7.5) added to each well and incubated with mixing at RT for 2 hrs in the dark. Fluorescence for hoescht staining read by microplate reader at excitation 355, emission 460.

Colony Formation Assays

4.0 x 10² cells were plated in 6-well plates and treated with indicated inhibitors for 14 days. Cells were then stained with crystal violet mixed with 10% formalin for 1 hr, washed with water, and imaged.

Transformation and Viral Infection

Competent Stbl3 bacteria were transformed with the lentiCRISPRv2 vector with or without target guides for GLS and FDX1 according to the lentiCRISPRv2 cloning protocol from

the Zhang lab [36]. 3.0×10^6 293T cells were plated 16-24 hours prior to transfection in 10 cm dishes. 6 μ g vector was added to 4 μ g Vsvg and 8 μ g 8.9 packaging plasmids in 500 μ L optimem and 90 μ L PEI was added to 500 μ L optimem, plasmid-containing solution was mixed with PEI-containing solution for 15 minutes at room temperature and added to 10 mL of 293T cell media. Media was changed 24 hours after transfection and collected and strained with 0.45 μ M cell strainers 48 hours later. 1.0 - 2.0×10^5 CWR-R1-EnzR cells were plated in 6-well plates 24 hours prior to transduction and 1 mL virus-containing media with 1:1000 polybrene was added to cells. Media was changed 24 hours after transduction and cells were treated with 1.2 μ g/mL puromycin for 4 days and maintained in media with puromycin for maintaining the knockout cell lines. CRISPR-Cas9 sgRNA sequences:

sgGLS #1 Forward: CACCGAAATTCAGTCCCGATTTGTG

sgGLS #1 Reverse: AAACCACAAATCGGGACTGAATTC

sgGLS #2 Forward: CACCGTCCATACACTCTTTCAACCT

sgGLS #2 Reverse: AAACAGGTTGAAAGAGTGTATGGAC

sgGLS #3 Forward: CACCGGACGCGTTTGGCAACAGCGA

sgGLS #3 Reverse: AAACCTCGCTGTTGCCAAACGCGTCC

sgFDX1 #1 Forward: CACCGGCAGGCCGCTGGATCCAGCG (as previously described in [37])

sgFDX1 #1 Reverse: AAACCGCTGGATCCAGCGGCCTGCC (as previously described in [37])

*sgFDX1 #2 Forward: CACCGTGATTCTCTGCTAGATGTTG (as previously described in [37])

*sgFDX1 #2 Reverse: AAACCAACATCTAGCAGAGAATCAC (as previously described in [37])

*Note: sgFDX1 #2 resulted in a consistently robust knockout of FDX1 in EnzS cells tested, but did not result in a consistently robust knockout of FDX1 in EnzR cells tested.

Animal Studies

2.50×10^5 CWR-R1-EnzR cells were injected subcutaneously into the flank of 4-6 week old male NOD-SCID mice in 75% PBS, 25% matrigel. Mice were castrated with bilateral orchiectomy six weeks post-implantation and treated with vehicle, CB-839, or elesclomol when tumor volume reached 100 mm³. CB-839 vehicle (25% HPBCD, 10 mM citrate, pH 2) and 20 mg/mL CB-839 were received from Calithera frozen in solution, thawed, aliquoted, stored at -80 C, syringe-filtered, and prepared fresh daily. Mice were treated with either vehicle or 200 mg/kg CB-839 by oral gavage twice daily for 42 days. Elesclomol powder was received by Accel Pharmtech. 40 mg/kg elesclomol was prepared in vehicle (5% DMSO, 40% PEG300, 5% Tween 80, 50% sterile water), aliquoted, stored at -80 C,

syringe-filtered, and thawed fresh for use daily. Mice were treated with vehicle or 40 mg/kg elesclomol daily IP, five days per week, for 28 days.

Explants

Fresh patient PCa tumors were cut into 1 mm³ pieces, put onto VETSPON absorbable hemostatic gelatin sponges and treated *ex vivo* with vehicle or 10 uM enzalutamide for 48 hrs in RPMI-1640 supplemented with 10% FBS, 1% penicillin-streptomycin, 10 ug/mL bovine insulin, and 10 ug/mL hydrocortisone in a 12-well plate at 37C.

Media Secretion Assays

1 mL of media was collected from cells at 80% confluence, analyzed by the NOVA BioProfile 4, and metabolite levels were normalized to protein content measured by BCA.

Immunoblot

Plates were washed with cold PBS and pellets resuspended in RIPA with protease and phosphatase inhibitors. Lysates were centrifuged at 14,000 rpm for 30 minutes, protein-containing supernatant transferred to new tubes, and flash frozen in liquid nitrogen. Protein was quantified by BCA and 30-40 ug was loaded into 4-20% Mini-PROTEAN TGX stain-free gels. Gels were transferred onto nitrocellulose membranes, blocked, and incubated in either anti-B-actin (Sigma, Catalog #: A5441, 1:5000 dilution), anti-GLS (Glutaminase C (GAC), Invitrogen, Catalog #: PA540135, 1:1000 dilution), anti-FDX1 (Proteintech, Catalog #: 12592-1-AP, 1:1000 dilution), anti-GLO1 (Santa Cruz Biotechnology, Catalog #: sc-133214 (D-5), 1:200 dilution), or anti-xCT/SLC7A11 (Cell Signaling Technology, Catalog #: 12691 (D2M7A1), 1:1000 dilution) overnight at 4C. Membranes were washed in PBS, and incubated in either anti-mouse IgG (Cell Signaling Technology, Catalog #: 7076) or anti-rabbit (Cell Signaling Technology, Catalog #: 7074) IgG HRP-linked secondary antibody at 1:3000 dilution for an hour at room temperature, washed with PBS and imaged.

qRT-PCR

100-500 ng/uL RNA extracted according to Qiagen RNeasy mini with spin technology protocol. 5.0×10^5 - 1.0×10^6 cells washed with cold PBS and harvested by scraping in 350 uL RLT buffer. 1 ug RNA used to make cDNA according to iScript RT protocol (5 min 25C, 20 min 46C, 1 min 95C, infinite hold at 4C). qRT-PCR run with supermix of 25 ng cDNA and 0.5 uM forward and 0.5 uM reverse primers according to the SYBR Green protocol (40 repeated cycles of 2 min 95C, 2 s 95C, 30 s 60C).

IHC

Mouse xenograft tissue was washed in cold PBS, formalin-fixed in 10% formalin-PBS, embedded in paraffin blocks, and 5 uM tissue slices were cut onto slides. Slides were dewaxed, dehydrated, and antigen retrieved with Vector citrate buffer (pH 6). Slides were blocked in Vector background sniper in humidified containers for an hour at room temperature and incubated with Ki67 primary antibody at a 1:1000 dilution (GeneTex, Catalog #: GTX16667 [SP6]) or cleaved caspase 3 (Asp175) (Cell Signaling Technology, Catalog #: 9661) primary antibody at a 1:300 dilution in Diamond solvent overnight in

humidified containers at 4°C. Slides were washed in PBS and incubated in biotinylated horse anti-rabbit secondary IgG (Vector Laboratories, Catalog #: BA-1100) at a 1:1000 dilution for Ki67 and a 1:500 dilution for cleaved caspase 3 in humidified containers for one hour at room temperature. Slides were developed with ImmPACT DAB after 25 second exposure after incubation with Vectastain ABC reagent and PBS washes. Slides were stained with hematoxylin and bluing reagent, rehydrated, mounted onto cover slips, dried, and imaged at 40x magnification.

Statistics

Data represents the mean or median of at least three biological replicates ($n = 3$) for each experiment, with error bars representing either standard deviation or standard error of the mean. The specific sample size of each experiment, error bar representation, and statistical test performed is noted in the figure legends. The data meet the assumptions of the statistical tests used, where the variance is similar between groups. Sample size was chosen for each experiment to detect a 33% increase or decrease with a standard deviation of 15% in order to achieve a power of 80% and p-value of 0.05. The number of mouse xenografts per cell line needed to detect a 33% decrease with a standard deviation of 15% in order to achieve a power of 80% and p-value of 0.05 was determined to be eight (four per group). The endpoints of animal studies were pre-established based on pilot experiments. All animals that completed the study were included. Animals were randomly assigned to each group, based on tumor size. Once animals reached the proper tumor size (around 100 mm³), they were started on treatment. The investigator was not blinded to the group allocation.

All experiments performed by flow cytometry are represented as median fluorescence intensity (MFI), while all other experiments are represented as means. For steady-state metabolomics, samples were normalized to total ion content and significance was calculated based on VIP scores greater than 1.0 generated by the UTSW metabolomics core or one factor statistics analysis software at <https://www.metaboanalyst.ca/> and $p < 0.05$ using unpaired t-tests and Mann-Whitney t-tests (for patient tissue metabolomics). Pathway analysis was performed using significantly altered metabolites with over-representation analysis with a cutoff of $p < 0.01$ and $q < 0.01$ with software from <http://cpdb.molgen.mpg.de/>. For stable isotope tracing experiments, significance was calculated based p-values < 0.05 using unpaired t-tests. Integrated pathway analysis of metabolomic and transcriptomic data performed using joint pathway analysis software from <https://www.metaboanalyst.ca/> with significantly altered genes from [29] and [30]. Identification of statistically significant gene alterations was determined by multiple t-tests with Benjamini, Krieger, and Yekutieli correction (FDR) with $q < 0.01$. Identification of significant metabolite alterations was determined by unpaired t-test with $p < 0.05$. For patient tumor transcriptome analysis, RNA-seq data was obtained from SU2C mCRPC study ($n = 159$). RNA-seq data for the RMH cohort ($n = 95$) was obtained as previously described [33]. Both mCRPC cohorts were analyzed as previous described [35]. TCGA ($n = 494$) data are available under Broad Institute GDAC TCGA Analysis Pipeline License. The expressed genes (median expression > 0 ; SU2C $n = 27945$; RMH = 30907; TCGA $n = 17708$) were ranked from high to low using the Spearman correlation coefficient between each gene's expression (fpkm) and glutamine/antioxidant target genes expression (fpkm), and

subsequently used for pathway analysis. Pathway analysis was performed using the Gene Set Enrichment Analysis (GSEA) Pre-Ranked algorithm from GSEA software (v4.1.0). To assess differences in mouse xenograft tumor growth, significance was determined by multiple t-tests with Benjamini, Krieger, and Yekutieli correction (FDR) with $q < 0.01$. All other significance was determined by unpaired t-test $p < 0.05$.

Study Approval

For experiments involving mice, all animals were housed and studies performed at UTSW, under the administration of the Animal Resource Center (ARC) and approved by the Institutional Animal Care and Use Committee (IACUC) under protocol number 2016-101380, in accordance with the NIH "Guide for Care and Use of Laboratory Animals." The UTSW IACUC uses the NIH "Guide for the Care and Use of Laboratory Animals" when establishing animal research standards. For experiments involving human tissue, human subjects were not used. Instead, de-identified clinical specimens from the UTSW Tissue Management Shared Resource was used and consented using IRB STU 102010-051, and labeled with a unique Tissue Management Shared Resource number and clinic-pathological characteristics. For RNA-seq experiments involving therapy-treated CRPC tumors from the Royal Marsden Hospital-Institute of Cancer Research (RMH-ICR, London, UK) ($n = 95$), all patients provided written consent, detailed information for this specific cohort can be found in previously published literature [33, 35]. No authors were able to correlate specific tissues to specific patients. Based on the NIH Human Subjects "Decision Tool," we have determined that this study involved only secondary research using data or biospecimens not collected specifically for this study and specimens or data will be provided without identifiable information by someone without any role in this research study except providing samples. Additionally, according to the NIH guide on "Research Involving Private Information or Biological Specimen," the recipient of this tissue cannot readily ascertain the identities of individuals to whom the specimens pertain. For these reasons, this research does not involve human subjects.

Results

Enzalutamide induces ROS in EnzS cells *in vitro* and in patient tumors *ex vivo*:

Using unbiased steady-state metabolomics, we compared the heatmaps of metabolic alterations in the EnzS cell line (LNCaP) under conditions of either AR agonism (treatment with synthetic AR agonist R1881 vs vehicle for cells grown in androgen-depleted media) or AR antagonism conditions (the combination of enzalutamide and R1881 vs R1881 for cells grown in androgen-depleted media) (Fig. 1A). Overlap analyses using venn diagrams indicated that 16 metabolites were inversely altered by AR agonism and AR antagonism for cells grown in androgen-depleted media. Pathway analysis of these 16 metabolites showed enrichment for metabolites involved in nucleotide, amino acid, and choline metabolism (Fig. 1B). Similarly, pathway analysis of the 34 metabolites altered with enzalutamide treatment (enzalutamide vs vehicle in cells grown in androgen-repleted media) identified enrichment in metabolites involved in nucleotide metabolism, amino acid metabolism, and the urea cycle (Fig. 1A, Supplementary Fig. 1A). Together, these unbiased metabolomic data identify

that enzalutamide treatment consistently induces alterations in nucleotide and amino acid metabolism.

We then integrated our metabolomic data with publically-available transcriptional datasets evaluating the effect of enzalutamide in LNCaP cells [29-32]. We first validated the effect of enzalutamide on canonical AR signaling in these datasets (Supplementary Fig. 1B-E). Integrative analyses with two distinct transcriptional datasets [29, 30] indicated that pathways involved in alanine/aspartate/glutamate metabolism and nitrogen metabolism were consistently and significantly altered (Fig. 1C-D, Supplementary Fig. 1F). The central role of glutamine metabolism was also supported by significant enrichment of pathways involved in glutathione (GSH) and glutamine/glutamate metabolism (Fig. 1C-D, Supplementary Fig. 1F). Since amino acid metabolism, especially glutamine metabolism, can regulate antioxidant levels [38], we then examined the regulation of genes involved in both glutamine and antioxidant metabolism. The transcriptomic analyses show that genes involved in both glutamine and antioxidant metabolism were induced by AR agonism and inhibited by AR antagonism (Fig. 1E-F) [29]. This finding of AR regulation was validated using two additional and distinct datasets [31, 32] (Supplementary Fig. 1G-H). Further, we have shown that SLC1A5, a canonical gene involved in glutamine transport, is both induced by AR agonism and inhibited by AR antagonism with enzalutamide (Supplementary Fig. 1I). Taken together, these data suggest that AR regulates genes involved in both glutamine and antioxidant metabolism and effectively regulates cancer redox homeostasis in PCa.

Analyses of two distinct AR ChIP-seq datasets show that all of the genes involved in glutamine and antioxidant metabolism (100%, 18/18) are proximal to AR binding peaks (Fig. 1G, Supplementary Fig. 1J) [26, 27]. Under normal androgenic conditions in LNCaP cells, the AR binding peaks are clearly evident (panel labeled normal growth media) (Fig. 1G, Supplementary Fig. 1J) [27]. Remarkably, these exact AR binding peaks in LNCaP cells were lost with blockade of AR signaling (panel labeled serum-starved media V) and rescued by treatment with R1881 (panel labeled serum-starved media R) in an independent AR ChIP-seq dataset (Fig. 1G, Supplementary Fig. 1J) [26]. Overlay of H3K27ac ChIP-seq [28] indicates that a majority (89%, 16/18) of these AR binding peaks are at or near active promoter or enhancer regions (Fig. 1G, Supplementary Fig. 1J). Since prior studies from our group have reported that AR binding sites can regulate multiple genes through chromatin looping [27], we leveraged RNA polymerase II CHIA-PET analyses to evaluate looping of AR peaks to sites of active transcription. Our 3-D genome analyses show that 83% (15/18) of these AR binding peaks loop to sites of active transcription. We noted that AR coordinately regulates three distinct genes (SLC38A1, SLC38A2, and SLC38A4) involved in glutamine metabolism via looping (Fig. 1G). We then validated this coordinated regulation, by showing a consistent positive correlation between the expression levels of these genes in three independent cohorts (mCRPC: SU2C-PCF (n = 159) and RMH-ICR (n = 95); Therapy-naïve: TCGA (n = 551) (Supplementary Fig. 1K). Together, these data robustly support our finding that genes involved in glutamine and antioxidant metabolism are directly regulated by AR.

To evaluate the impact of AR signaling on antioxidant programs, we then evaluated the effect of AR antagonism with enzalutamide on ROS using flow cytometry-based general

oxidative stress assays. We demonstrated that enzalutamide induced ROS in AR-expressing LNCaP and C4-2B cells but not in AR-null PC-3 cells (Fig. 1H-J). In contrast, AR agonism with R1881 inhibited both the basal and enzalutamide-induced ROS in LNCaP cells (Fig. 1K). These findings are supported by metabolic evaluation of the effect of AR modulation on the ratio of oxidized (GSSG) and reduced glutathione (GSH) and S-lactoylglutathione levels (Fig. 1L-M, Supplementary Fig. 1L). Consistent with its ability to induce ROS, enzalutamide treatment enhances the GSSH:GSH ratio (Fig. 1M). Increased ROS inhibits glyoxylase I (GLO1) (which catalyzes the conversion of GSH to S-lactoylglutathione, as shown in Fig. 1L), resulting in lower S-lactoylglutathione levels [39-41]. We noted that enzalutamide decreases androgen-induced S-lactoylglutathione levels (Supplementary Fig. 1L). These data support our finding that enzalutamide induces ROS in PCa *in vitro* and clearly demonstrated that ROS regulation in PCa cells is AR-dependent.

To validate the *in vitro* findings, we then adapted our *ex vivo* culture methodology to perform ROS assays in primary, treatment-naïve patient tumors [42] (Table 1). Fresh extirpated PCa tumors were cultured *ex vivo* with either vehicle or enzalutamide, collagenase digested, and processed for flow cytometry to evaluate ROS levels (Fig. 1N). These data demonstrate for the first time the feasibility of ROS evaluation in primary tumors and showed that enzalutamide induced oxidative stress in primary PCa tumors (Fig. 1O). Since most primary PCa tumors are AR-dependent and sensitive to enzalutamide, these observations also support our central finding that inhibition of AR in PCa induces ROS. Taken together, these data indicate that enzalutamide induces oxidative stress by reducing antioxidants in PCa *in vitro* and *ex vivo*.

EnzR cells and antiandrogen-treated CRPC tumors have increased basal and inducible ROS:

We next evaluated transcriptional programs in patient tumors after enzalutamide treatment. Since a true matched cohort of patient tumors from the same patient before and after enzalutamide treatment is not available, we compared transcriptional programs from a dataset of 494 treatment-naïve primary PCa tumors from the cancer genome atlas (TCGA) to 95 CRPC tumors obtained after treatment with second-generation antiandrogens, enzalutamide and abiraterone, from the Royal Marsden Hospital-Institute for Cancer Research (RMH-ICR) (Fig. 2A, Supplementary Fig. 2A). Using pathway enrichment analysis, we found that the expression of AR-regulated glutamine and antioxidant metabolism genes positively correlated with oxidative stress pathways in antiandrogen-treated CRPC tumors, but not in therapy-naïve primary PCa tumors (Fig. 2A, Supplementary Fig. 2B). Glutaminase (GLS) expression specifically correlated with oxidative stress pathways in antiandrogen-treated CRPC tumors but not primary therapy-naïve tumors (Fig. 2A, Supplementary Fig. 2B). These data support our *in vitro* findings that glutamine and antioxidant metabolism pathways are important for ROS regulation following AR-targeted therapy in CRPC.

From analyses of microarray data, we found that the basal expression levels for most (81% (13/16)) enzalutamide-regulated genes involved in glutamine and antioxidant metabolism were comparable between paired EnzS cells and EnzR cells (Supplementary Fig. 2C-D)

[22]. This finding is not surprising given that enzalutamide resistance is associated with restoration of the expression of canonical AR-regulated genes [22].

To directly assess the association between oxidative stress and therapy resistance, general oxidative stress was measured in fresh primary treatment-naïve and CRPC patient tumors using flow cytometry (Supplementary Fig. 2A, Table 2). We consistently detected a higher basal level of ROS in CRPC tumors (n = 5), compared to therapy-naïve primary tumors (n = 6, Fig. 2B). Further, following treatment with oxidizing agent, hydrogen peroxide (H₂O₂), the inducible levels of ROS and fold induction was higher in CRPC tumors, compared to therapy-naïve primary tumors (Fig. 2B). Steady-state metabolic evaluation of a cohort of primary therapy-naïve (n = 19) and CRPC tumors from either the prostate (n = 9) or metastatic sites (n = 6) (Table 3) showed a significant alteration in 112 metabolites and an over-representation in oxidative stress pathways (Supplementary Fig. 2A and 2E). Targeted metabolic profiling using a formic acid extraction to stabilize labile metabolites (like GSH) demonstrated that CRPC tumors had an increased GSSG:GSH ratio caused by a GSH pool depletion and indicated increased ROS (Fig. 2C, Supplementary Fig. 2F). We also noted that metastatic tumors had an increased GSSG:GSH ratio, compared to localized tumors (Fig. 2D-E, Supplementary Fig. 2G). Further, organoids derived from EnzR patients had a depleted GSH pool, compared to organoids derived from EnzS LNCaP cells (the lack of EnzS patient-derived organoids precluded a true comparison of GSH levels) (Fig. 2F). Taken together, our data indicate that basal oxidative stress levels correlate with disease progression and treatment with antiandrogen therapy.

We then evaluated three matched pairs of validated EnzS and EnzR cells (LNCaP, C4-2B, and CWR-R1) (Supplementary Fig. 2H) [22-24]. Using fluorescence microscopy (Fig. 2G) and flow cytometry assays (Fig. 2H), we found that EnzR cells had both a higher basal level of oxidative stress and increased H₂O₂-induced ROS inducibility, compared to matched EnzS cells. Both relative and quantitative steady-state metabolomics (Fig. 2I, Supplementary Fig. 2I) and flow cytometry-based assays (Fig. 2J) demonstrated that EnzR cells had a depleted GSH pool and an increased GSSG:GSH ratio, compared to EnzS cells. Further, EnzR cells also have reduced GLO1 expression and decreased S-lactoylglutathione levels, compared to EnzS cells (Supplementary Fig. 2J-K). EnzR cells neither have a decreased glycolytic rate (as measured by lactate secretion) associated with the reduction in S-lactoylglutathione (Supplementary Fig. 2L) [43], nor have associated changes in lipid peroxides, xCT levels, erastin sensitivity, NRF2 signaling, or mitochondrial content (Supplementary Fig. 2M-Q). These data demonstrate that EnzR cells and therapy-resistant patient tumors have increased basal and inducible ROS.

EnzR cells and CRPC tumors have enhanced glutamine metabolism:

We performed steady-state metabolic profiling in six matched pairs of EnzS and EnzR cell lines (CWR-R1, C4-2B, LAPC-4) and three LNCaP cell lines independently derived at three different institutions [22-24]. Heatmaps highlight significant differences in metabolites between EnzS and EnzR cell lines under normal growth conditions (Fig. 3A). Unsupervised clustering showed that EnzR cells were metabolically similar and distinct from EnzS cells (Fig. 3A). Pathway analysis of all significantly altered metabolites (FC > 2) in each pair

identified that amino acid metabolism was consistently altered in all six pairs of EnzR cells (Fig. 3B-C, Supplementary Fig. 3A). Overlap analysis of either the three EnzS/EnzR LNCaP pairs or the three different EnzS/EnzR cell line pairs validated that amino acid metabolism was the most frequently altered pathway in EnzR cells (Fig. 3D-E). Individual profiling of each amino acid (Supplementary Fig. 3B) identified that glutamine was upregulated in most EnzR cell lines (Fig. 3F). Since glutamate is derived from glutamine, we noted in those EnzR cell lines where glutamine was not significantly upregulated, that glutamate was upregulated (Fig. 3F). Thus, all EnzR cells are consistently seen to have an increase in glutamine or glutamate levels. We then noted that EnzR cells also had increased glutamate secretion (relative to glutamine), (Supplementary Fig. 3C). ¹³C-glutamine tracing experiments show that EnzR cells have an enhanced preference for utilizing glutamine to make GSH. (Fig. 3G-H). These stable isotope tracing experiments also indicate that EnzR cells have enhanced GLS activity to more rapidly synthesize glutamate from glutamine, (Supplementary Fig. 3D). Importantly, a similar phenotype was seen in patient tumor specimens, where CRPC tumors had higher levels of glutamine, compared to primary, therapy-naïve tumors (Fig. 3I-J). Furthermore, GLS expression positively correlated with oxidative stress pathways in antiandrogen-treated CRPC tumors but not in therapy-naïve tumors (Fig. 2A, Supplementary Fig. 2B). These data demonstrate that EnzR cells and therapy-treated patient tumors have enhanced glutamine metabolism.

EnzR cells are vulnerable to glutamine blockade:

To test the glutamine dependence of EnzR cells, proliferation assays were performed in the presence and absence of glutamine. Compared to EnzS cells, EnzR cells were more sensitive to glutamine but not glucose deprivation (Fig. 4A, Supplementary Fig. 4A). CB-839, a small-molecule inhibitor of GLS, inhibited proliferation ($IC_{50} < 0.05 \mu M$) and colony formation in EnzR cells to a greater degree than in EnzS cells (Fig. 4B-C). Importantly, CB-839 inhibited glutamate levels and selectively induced ROS in EnzR cells but not in EnzS cells, as shown by ROS assays and inhibition of S-lactoylglutathione levels (Fig. 4D-E, Supplementary Fig. 4B-C). The ability of an antioxidant, N-acetylcysteine (NAC), to rescue the anti-proliferative effects of CB-839 in EnzR cells indicated that CB-839 inhibited proliferation through ROS induction (Fig. 4F). CRISPR-Cas9-mediated knockout of GLS was sufficient to induce ROS in both EnzS and EnzR CWR-R1 cells (Fig. 4G-H, Supplementary Fig. 4D-E). Loss of GLS had a more profound inhibition of growth of EnzR cells than EnzS cells (Fig. 4G and 4I, Supplementary Fig. 4D and 4F-G). Oral administration of CB-839 inhibited the growth of EnzR xenografts *in vivo*, with no effect on mouse body weight (Fig. 4J, Supplementary Fig. 4H-I). The xenograft tumor proliferative indices (measured by Ki67 staining) was significantly decreased in the CB-839-treated mice (Fig. 4K). Steady-state metabolomics of extirpated tumors demonstrated that CB-839 increased intratumoral glutamine and decreased glutamate (Fig. 4L, Supplementary Fig. 4J). Evaluation of EnzR xenografts showed that CB-839 induced ROS (Fig. 4M). Since GLS was also shown to play a role in ROS regulation in antiandrogen-treated CRPC tumors but not therapy-naïve tumors (Fig. 2A, Supplementary Fig. 2B), our data show that CB-839 blocks glutamine-dependent antioxidant programs and consequently EnzR-PCa growth *in vitro* and *in vivo*.

EnzR cells are vulnerable to ferredoxin blockade:

Our data indicate that cellular antioxidant programs are critical for the survival of EnzR-PCa cells and tumors. Evaluation of patient tumors identified that another driver of cellular antioxidant programs, ferredoxin 1 (FDX1), was also associated with ROS regulation in antiandrogen-treated CRPC but not therapy-naïve tumors (Fig. 2A, Supplementary Fig. 2B). We showed that EnzR cells were more sensitive than EnzS cells to an FDX1-selective small-molecule inhibitor, elesclomol [37], by proliferation, colony formation, and apoptotic assays. (Fig. 5A-C). Elesclomol induced ROS selectively in EnzR but not in EnzS cells (Fig. 5D, Supplementary Fig. 5A). The anti-proliferative effect of elesclomol in EnzR cells was mediated by ROS, as evidenced by the ability of the antioxidant, NAC, to rescue EnzR proliferation (Fig. 5E). In addition, loss of FDX1 (through CRISPR-mediated knockout) was sufficient to induce ROS and inhibit cell viability in EnzS and EnzR cells (Fig. 5F-H, Supplementary Fig. 5B-D). Again, the loss of FDX1 more significantly inhibited EnzR cell growth than EnzS growth (Supplementary Fig. 5E). Critically, the effect of elesclomol on EnzR growth was validated *in vivo*, as shown by the inhibition of tumor growth and proliferation (measured by Ki67 staining) of EnzR xenografts in mice, with no effect on body weight (Fig. 5I-J, Supplementary Fig. 5F-G). Similar to its *in vitro* effect, elesclomol also induced apoptosis *in vivo* (as measured by cleaved caspase 3 staining) (Supplementary Fig. 5H). Elesclomol-treated xenografts displayed an induction of ROS, compared to vehicle-treated xenografts (Fig. 5K). These data together suggest that the antioxidant role of FDX1 is important for EnzR-PCa survival, and can be targeted therapeutically.

Discussion

This is the first study, to our knowledge, to comprehensively characterize the metabolic alterations associated with enzalutamide resistance in therapy-sensitive and therapy-resistant PCa cells, mouse xenografts, organoids, and patient tumors. Using transcriptomics, metabolomics, fluorescence microscopy, and flow cytometry-based assays, we report the novel finding that EnzR-PCa cells have increased basal and inducible levels of oxidative stress than their EnzS-PCa counterparts. We have also shown that enzalutamide induces ROS by regulating antioxidant genes in an androgen-dependent manner in both “hormone-sensitive” PCa cell lines and primary patient-derived PCa explants. Our findings build on reports that castration can induce oxidative stress in androgen-dependent rat prostate epithelial cells, and transient knockdown of AR in androgen-dependent PCa cell lines can induce ROS [30, 44], and show for the first time a difference in ROS levels in EnzS and EnzR-PCa cells. In contrast, other studies have shown that in “CRPC” cell lines, like 22Rv1, androgens induce ROS [45, 46]. The increased ROS in response to androgens in 22Rv1 cells is likely to be related to the androgen-independent nature of this cell line and may reflect the differential and contextual effect of androgens on ROS in different stages of disease (HSPC vs CRPC). Given that 22Rv1 cells concomitantly express various AR variants [47], we speculate that for some AR variants, androgens may serve as antagonists, and thereby block AR signaling culminating in ROS induction. We suggest that the multiple AR variants in 22Rv1 cells may exhibit differential genome-wide occupancy and this can be further influenced by the presence of androgens. Future work on 22Rv1 cells should test these hypotheses.

We validated these findings in patient tumors and showed that CRPC patient tumors have a higher basal level of ROS and greater ROS inducibility than therapy-naïve primary PCa tumors. Our analyses of transcriptomic datasets validated that AR-regulated antioxidant metabolism genes positively correlate with oxidative stress pathways in CRPC patients treated with enzalutamide and abiraterone but not in primary treatment-naïve PCa tumors. Metabolic profiling of primary therapy-naïve and CRPC PCa patient tumors demonstrated that CRPC tumors have a depleted GSH pool and a corresponding increased GSSG:GSH ratio, indicative of increased ROS. Overall, these data support our finding of differences in both basal and inducible levels of ROS in EnzS (therapy-naïve) versus EnzR (CRPC) tumors.

Our studies showed that a subset of glutamine metabolism genes are AR-regulated and correlate with oxidative stress pathways in CRPC patient tumors but not therapy-naïve tumors. The unequivocal overlap of AR DNA binding peaks near the transcriptionally active promoters of these genes in two independent AR ChIP-seq studies defines a bonafide cis-tromic regulation. Further, the coordinated regulation of three glutamine metabolism genes (SLC38A1, SLC38A2, and SLC38A4) identified from 3-D genomic evaluation of AR looping and validated in patient tumor samples, establishes that these genes are clearly directly AR-regulated.

Importantly, using unbiased metabolic profiling of paired EnzS/EnzR PCa cells and therapy-naïve and therapy-resistant patient tumors, we found that therapy-resistant PCa had enhanced glutamine metabolism, which is used to generate GSH. Increasing glutamine metabolism is likely an antioxidant mechanism utilized by EnzR-PCa to tolerate greater oxidative stress and prevent ROS-mediated cell death.

We have shown that EnzR cells are more glutamine-dependent and GLS inhibition with small-molecule inhibitors or GLS loss is sufficient for ROS induction and inhibition of EnzR-PCa growth in cells and xenografts. Our work is supported by previous studies, which have shown a role for several different glutamine metabolism genes in PCa in various contexts. AR, mTOR, and MYC have all been shown to increase glutamine uptake and utilization in PCa cells, mainly mediated by glutamine transporters [48, 49]. GLS has been shown to play a role in many cancers, including triple-negative breast cancer, non-small cell lung cancer, and glioma, and small-molecule inhibitors of GLS alone and in combination with other therapies have been proposed as a strategy to improve patient responses [50-52]. Although GLS expression in patient tumors does not seem to be predictive of PCa tumorigenesis or PCa stage [53], different GLS isoforms have been characterized in PCa cells and patient tumors, and previous studies have posited that GLS isoform switching may play a role in the development of CRPC [49]. A phase II clinical trial investigating the effect of the combination of CB-839 with a PARP inhibitor, talazoparib, in metastatic CRPC was opened and has not yet begun recruiting patients ([NCT04824937](https://clinicaltrials.gov/ct2/show/study/NCT04824937)). Taken together, we propose that because EnzR-PCa has a greater basal ROS and increased ROS inducibility, ROS induction by glutamine blockade may represent a therapeutic strategy to target EnzR-PCa.

This study demonstrates that EnzR cells and CRPC tumors have a programmatic shift that creates a new vulnerability to ROS induction by antioxidant inhibition, and is a potentially viable therapeutic strategy to target EnzR-PCa. Enzalutamide resistance in PCa is likely driven by tolerance to oxidative stress, and this vulnerability can be targeted by blocking antioxidant programs in either a glutamine-dependent or a glutamine-independent manner (Fig. 5L).

Our studies suggest that EnzR cells become more glutamine-dependent to tolerate the ROS induced by enzalutamide, are dependent on antioxidant programs, and develop a vulnerability to glutamine and ferredoxin metabolism inhibition. Our data indicates that ferredoxin metabolism is an important antioxidant program for EnzR-PCa survival. Ferredoxin inhibitors, such as elesclomol, may be useful for targeting cancer cells with an increased mitochondrial dependence [37, 54, 55], which tend to rely more on glutamine for normal mitochondrial function and ATP synthesis [56, 57]. Consistent with this idea, forcing EnzS cells to become dependent on their mitochondria through glucose deprivation and galactose supplementation (Hi-Mito) causes these cells to be just as sensitive to elesclomol as EnzR cells (Supplementary Fig. 5I).

The role of FDX1 in iron-sulfur (Fe-S) cluster formation may explain why EnzR cells are exquisitely sensitive to ROS induction. Fe-S cluster formation and attachment onto acceptor proteins in the mitochondrial membrane by the iron-sulfur cluster (ISC) complex is integral for electron transfer chain (ETC) function, steroidogenesis, bile acid, and vitamin D metabolism, and overall critical for mitochondrial function [58-62]. Given the established link between enhanced ferredoxin metabolism and sensitivity to ROS induction, increased FDX1 expression or activity in EnzR-PCa may account for the greater ROS inducibility with H₂O₂ observed and increased sensitivity to compounds that induce ROS, such as elesclomol and CB-839 [63-66]. Further mechanistic studies are needed to understand the role of FDX1 in prostate epithelial cells to obtain greater clarity on its function as an antioxidant and other critical roles it may have in steroidogenesis and mitochondrial pathways.

Taken together, these findings in PCa cell lines, mouse xenografts, patient-derived organoids, and patient tumors indicate that enzalutamide resistance in PCa is driven by tolerance to oxidative stress mediated by enhanced antioxidant programs, and this is targetable through glutamine blockade or ferredoxin inhibition.

Supplementary Material

Refer to Web version on PubMed Central for supplementary material.

Acknowledgments

We would like to thank Lauren Zacharias, Hieu Vieu, Duyen Do, and the Children's Research Institute Metabolomic core for their assistance with metabolic assays and analysis, as well as the Children's Research Institute Flow Cytometry core and UTSW Live Cell Imaging core for providing training and equipment for microscopy and flow cytometry experiments. We also thank the Simmon's Cancer Center's Tissue Management Shared Resource, which provided the patient tissue reported in this publication with support from National Cancer Institute of the NIH award no. P30CA142543. Additionally, we would like to thank Jer-Tsong (JT) Hsieh, Donald Vander Griend, and Amina Zoubeidi for providing cell lines for this study. Additional thanks goes to Tracy Rosales for providing helpful information and advice on experiments involving glutaminase and glutamine metabolism.

Funding Sources:

The National Cancer Institute at the National Institutes of Health Grant 1F31CA243276-01A1 and the Cancer Prevention and Research Institute of Texas Grant RP160157 (EBB). The National Cancer Institute at the National Institutes of Health Grant T32CA124334 (KP). Simmons Cancer Center at UT Southwestern for the Prostate Cancer Program, the Mimi and John Cole Prostate Cancer Fund, the Prostate Cancer Foundation, the Jasper L. and Jack Denton Wilson Foundation, and the Department of Defense Grants W81XWH-17-1-0674, W81XWH-19-1-0363, and W81XWH-21-1-0687 (GVR). RSM acknowledges funding support from National Cancer Institute (NCI)/NIH grant (R01CA245294), Cancer Prevention and Research Institute of Texas (CPRIT) Individual Investigator Research Award (RP190454), and US Department of Defense Breakthrough Award (W81XWH-21-1-0114).

Data Availability Statement

All data generated or analyzed during this study are included in this published article and corresponding supplementary information files. Any additional datasets generated during and/or analyzed during this study are available from the corresponding author upon reasonable request.

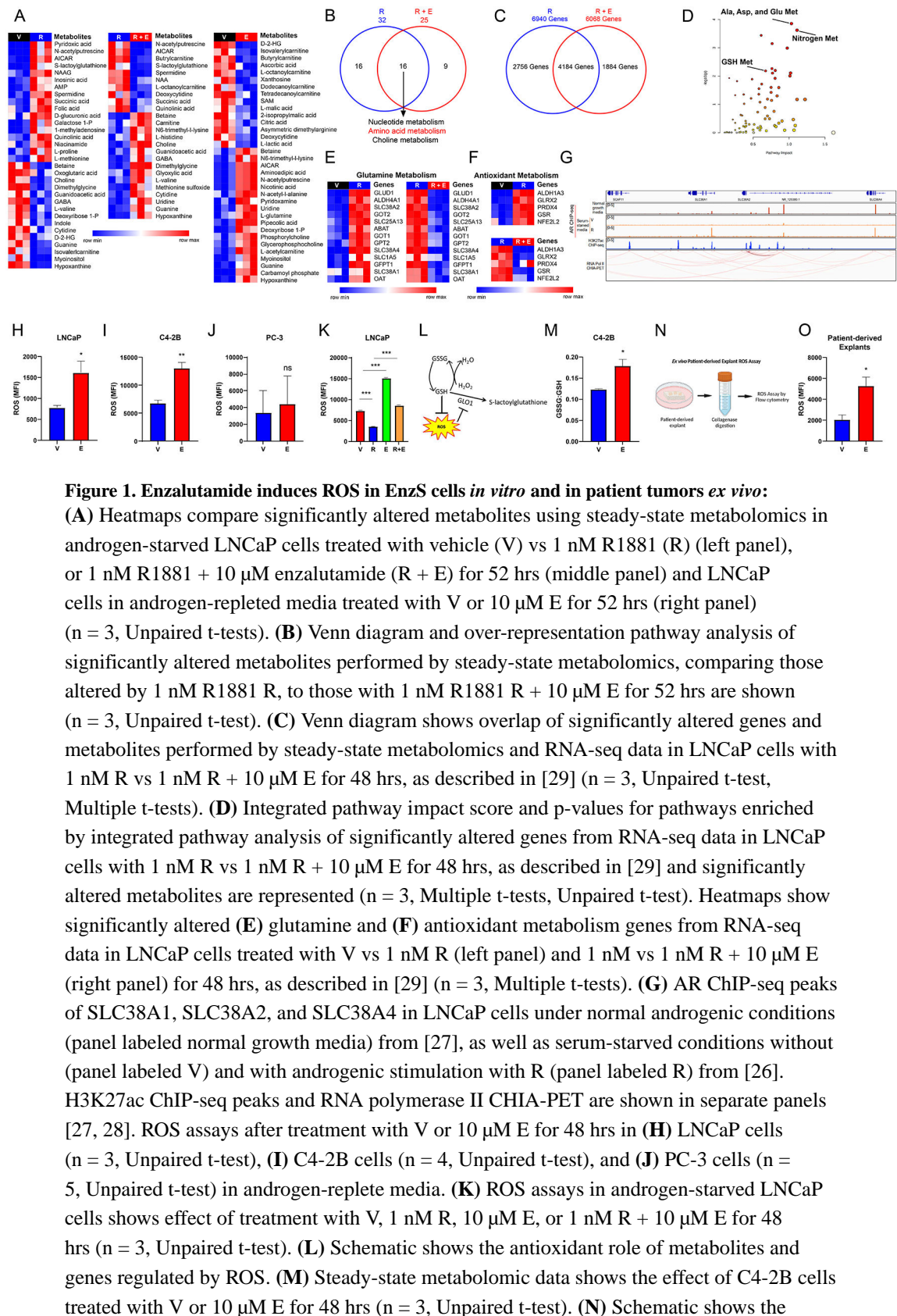
References

1. Abida W, Cyrta J, Heller G, Prandi D, Armenia J, Coleman I, et al. , Genomic correlates of clinical outcome in advanced prostate cancer. *Proc Natl Acad Sci U S A*, 2019. 116(23): p. 11428–11436. [PubMed: 31061129]
2. Chen CD, Welsbie DS, Tran C, Baek SH, Chen R, Vessella R, et al. , Molecular determinants of resistance to antiandrogen therapy. *Nat Med*, 2004. 10(1): p. 33–9. [PubMed: 14702632]
3. Robinson D, Van Allen EM, Wu YM, Schultz N, Lonigro RJ, Mosquera JM, et al. , Integrative clinical genomics of advanced prostate cancer. *Cell*, 2015. 161(5): p. 1215–1228. [PubMed: 26000489]
4. Maximum androgen blockade in advanced prostate cancer: an overview of the randomised trials. Prostate Cancer Trialists' Collaborative Group. *Lancet*, 2000. 355(9214): p. 1491–8. [PubMed: 10801170]
5. Huggins C, Prostatic cancer treated by orchiectomy; the five year results. *J Am Med Assoc*, 1946. 131: p. 576–81. [PubMed: 20986021]
6. Liu J, Geller J, Albert J, and Kirshner M, Acute effects of testicular and adrenal cortical blockade on protein synthesis and dihydrotestosterone content of human prostate tissue. *J Clin Endocrinol Metab*, 1985. 61(1): p. 129–33. [PubMed: 2581988]
7. Mercader M, Sengupta S, Bodner BK, Manecke RG, Cosar EF, Moser MT, et al. , Early effects of pharmacological androgen deprivation in human prostate cancer. *BJU Int*, 2007. 99(1): p. 60–7. [PubMed: 17227493]
8. Mohler JL, Gregory CW, Ford OH 3rd, Kim D, Weaver CM, Petrusz P, et al. , The androgen axis in recurrent prostate cancer. *Clin Cancer Res*, 2004. 10(2): p. 440–8. [PubMed: 14760063]
9. Montironi R, Magi-Galluzzi C, Muzzonigro G, Prete E, Polito M, and Fabris G, Effects of combination endocrine treatment on normal prostate, prostatic intraepithelial neoplasia, and prostatic adenocarcinoma. *J Clin Pathol*, 1994. 47(10): p. 906–13. [PubMed: 7525657]
10. Mostaghel EA, Page ST, Lin DW, Fazli L, Coleman IM, True LD, et al. , Intraprostatic androgens and androgen-regulated gene expression persist after testosterone suppression: therapeutic implications for castration-resistant prostate cancer. *Cancer Res*, 2007. 67(10): p. 5033–41. [PubMed: 17510436]
11. Ohlson N, Wikström P, Stattin P, and Bergh A, Cell proliferation and apoptosis in prostate tumors and adjacent non-malignant prostate tissue in patients at different time-points after castration treatment. *Prostate*, 2005. 62(4): p. 307–15. [PubMed: 15389788]
12. Chi KN, Chowdhury S, Bjartell A, Chung BH, Pereira AJ de Santana Gomes R. Given, et al. , Apalutamide in Patients With Metastatic Castration-Sensitive Prostate Cancer: Final Survival

- Analysis of the Randomized, Double-Blind, Phase III TITAN Study. *J Clin Oncol*, 2021. 39(20): p. 2294–2303. [PubMed: 33914595]
13. Fizazi K, Shore ND, Smith MR, Ramos R, Jones RJ, Niegisch G, et al. , Efficacy and safety outcomes of darolutamide in patients with nonmetastatic castration-resistant prostate cancer with comorbidities and concomitant medications from ARAMIS. *Journal of Clinical Oncology*, 2022. 40(6_suppl): p. 256–256.
 14. Fizazi K, Shore ND, Tammela T, Ulys A, Vjaters E, Polyakov S, et al. , ARAMIS: Efficacy and safety of darolutamide in nonmetastatic castration-resistant prostate cancer (nmCRPC). *Journal of Clinical Oncology*, 2019. 37(7_suppl): p. 140–140.
 15. Gourd E, Apalutamide shows efficacy in prostate cancer. *Lancet Oncol*, 2018. 19(3): p. e149. [PubMed: 29456088]
 16. Hussain M, Fizazi K, Saad F, Rathenborg P, Shore N, Ferreira U, et al. , Enzalutamide in Men with Nonmetastatic, Castration-Resistant Prostate Cancer. *N Engl J Med*, 2018. 378(26): p. 2465–2474. [PubMed: 29949494]
 17. Komura K, Fujiwara Y, Uchimoto T, Saito K, Tanda N, Matsunaga T, et al. , Comparison of Radiographic Progression-Free Survival and PSA Response on Sequential Treatment Using Abiraterone and Enzalutamide for Newly Diagnosed Castration-Resistant Prostate Cancer: A Propensity Score Matched Analysis from Multicenter Cohort. *J Clin Med*, 2019. 8(8).
 18. Tran C, Ouk S, Clegg NJ, Chen Y, Watson PA, Arora V, et al. , Development of a second-generation antiandrogen for treatment of advanced prostate cancer. *Science*, 2009. 324(5928): p. 787–90. [PubMed: 19359544]
 19. Farber S, Some observations on the effect of folic acid antagonists on acute leukemia and other forms of incurable cancer. *Blood*, 1949. 4(2): p. 160–7. [PubMed: 18107667]
 20. Noordhuis P, Holwerda U, Van der Wilt CL, Van Groenigen CJ, Smid K, Meijer S, et al. , 5-Fluorouracil incorporation into RNA and DNA in relation to thymidylate synthase inhibition of human colorectal cancers. *Ann Oncol*, 2004. 15(7): p. 1025–32. [PubMed: 15205195]
 21. Werkheiser WC, Specific Binding of 4-Amino Folic Acid Analogues by Folic Acid Reductase. *Journal of Biological Chemistry*, 1961. 236: p. 888–893.
 22. Kregel S, Chen JL, Tom W, Krishnan V, Kach J, Brechka H, et al. , Acquired resistance to the second-generation androgen receptor antagonist enzalutamide in castration-resistant prostate cancer. *Oncotarget*, 2016. 7(18): p. 26259–74. [PubMed: 27036029]
 23. Bishop JL, Thaper D, Vahid S, Davies A, Ketola K, Kuruma H, et al. , The Master Neural Transcription Factor BRN2 Is an Androgen Receptor-Suppressed Driver of Neuroendocrine Differentiation in Prostate Cancer. *Cancer Discov*, 2017. 7(1): p. 54–71. [PubMed: 27784708]
 24. Liu C, Lou W, Zhu Y, Nadiminty N, Schwartz CT, Evans CP, et al. , Niclosamide inhibits androgen receptor variants expression and overcomes enzalutamide resistance in castration-resistant prostate cancer. *Clin Cancer Res*, 2014. 20(12): p. 3198–3210. [PubMed: 24740322]
 25. Drost J, Karthaus WR, Gao D, Driehuis E, Sawyers CL, Chen Y, et al. , Organoid culture systems for prostate epithelial and cancer tissue. *Nat Protoc*, 2016. 11(2): p. 347–58. [PubMed: 26797458]
 26. Stelloo S, Nevedomskaya E, Kim Y, Hoekman L, Bleijerveld OB, Mirza T, et al. , Endogenous androgen receptor proteomic profiling reveals genomic subcomplex involved in prostate tumorigenesis. *Oncogene*, 2018. 37(3): p. 313–322. [PubMed: 28925401]
 27. Ramanand SG, Chen Y, Yuan J, Daescu K, Lambros MB, Houlahan KE, et al. , The landscape of RNA polymerase II-associated chromatin interactions in prostate cancer. *J Clin Invest*, 2020. 130(8): p. 3987–4005. [PubMed: 32343676]
 28. Taberlay PC, Achinger-Kawecka J, Lun AT, Buske FA, Sabir K, Gould CM, et al. , Three-dimensional disorganization of the cancer genome occurs coincident with long-range genetic and epigenetic alterations. *Genome Res*, 2016. 26(6): p. 719–31. [PubMed: 27053337]
 29. Yang Z, Wang D, Johnson JK, Pascal LE, Takubo K, Avula R, et al. , A Novel Small Molecule Targets Androgen Receptor and Its Splice Variants in Castration-Resistant Prostate Cancer. *Mol Cancer Ther*, 2020. 19(1): p. 75–88. [PubMed: 31554654]
 30. Gillis JL, Hinneh JA, Ryan NK, Irani S, Moldovan M, Quek LE, et al. , A feedback loop between the androgen receptor and 6-phosphogluconate dehydrogenase (6PGD) drives prostate cancer growth. *Elife*, 2021. 10.

31. Geng H, Xue C, Mendonca J, Sun XX, Liu Q, Reardon PN, et al. . Interplay between hypoxia and androgen controls a metabolic switch conferring resistance to androgen/AR-targeted therapy. *Nat Commun*, 2018. 9(1): p. 4972. [PubMed: 30478344]
32. Poluri RTK, Paquette V, Allain É P, Lafront C, Joly-Beauparlant C, Weidmann C, et al. . KLF5 and NFYA factors as novel regulators of prostate cancer cell metabolism. *Endocr Relat Cancer*, 2021. 28(4): p. 257–271. [PubMed: 33690159]
33. Fenor de la Maza MD, Chandran K, Rekowski J, Shui IM, Gurel B, Cross E, et al. . Immune Biomarkers in Metastatic Castration-resistant Prostate Cancer. *Eur Urol Oncol*, 2022.
34. Nava Rodrigues D, Rescigno P, Liu D, Yuan W, Carreira S, Lambros MB, et al. . Immunogenomic analyses associate immunological alterations with mismatch repair defects in prostate cancer. *J Clin Invest*, 2018. 128(10): p. 4441–4453. [PubMed: 30179225]
35. Sharp A, Coleman I, Yuan W, Sprenger C, Dolling D, Rodrigues DN, et al. . Androgen receptor splice variant-7 expression emerges with castration resistance in prostate cancer. *J Clin Invest*, 2019. 129(1): p. 192–208. [PubMed: 30334814]
36. Sanjana NE, Shalem O, and Zhang F, Improved vectors and genome-wide libraries for CRISPR screening. *Nat Methods*, 2014. 11(8): p. 783–784. [PubMed: 25075903]
37. Tsvetkov P, Detappe A, Cai K, Keys HR, Brune Z, Ying W, et al. . Mitochondrial metabolism promotes adaptation to proteotoxic stress. *Nat Chem Biol*, 2019. 15(7): p. 681–689. [PubMed: 31133756]
38. Sappington DR, Siegel ER, Hiatt G, Desai A, Penney RB, Jamshidi-Parsian A, et al. . Glutamine drives glutathione synthesis and contributes to radiation sensitivity of A549 and H460 lung cancer cell lines. *Biochim Biophys Acta*, 2016. 1860(4): p. 836–43. [PubMed: 26825773]
39. Birkenmeier G, Stegemann C, Hoffmann R, Günther R, Huse K, and Birkemeyer C, Posttranslational modification of human glyoxalase 1 indicates redox-dependent regulation. *PLoS One*, 2010. 5(4): p. e10399. [PubMed: 20454679]
40. Fratelli M, Demol H, Puype M, Casagrande S, Villa P, Eberini I, et al. . Identification of proteins undergoing glutathionylation in oxidatively stressed hepatocytes and hepatoma cells. *Proteomics*, 2003. 3(7): p. 1154–61. [PubMed: 12872216]
41. Hollenbach M, Hintersdorf A, Huse K, Sack U, Bigl M, Groth M, et al. . Ethyl pyruvate and ethyl lactate down-regulate the production of pro-inflammatory cytokines and modulate expression of immune receptors. *Biochem Pharmacol*, 2008. 76(5): p. 631–44. [PubMed: 18625205]
42. Centenera MM, Hickey TE, Jindal S, Ryan NK, Ravindranathan P, Mohammed H, et al. . A patient-derived explant (PDE) model of hormone-dependent cancer. *Mol Oncol*, 2018. 12(9): p. 1608–1622. [PubMed: 30117261]
43. Luengo A, Abbott KL, Davidson SM, Hosios AM, Faubert B, Chan SH, et al. . Reactive metabolite production is a targetable liability of glycolytic metabolism in lung cancer. *Nat Commun*, 2019. 10(1): p. 5604. [PubMed: 31811141]
44. Tam NN, Gao Y, Leung YK, and Ho SM, Androgenic regulation of oxidative stress in the rat prostate: involvement of NAD(P)H oxidases and antioxidant defense machinery during prostatic involution and regrowth. *Am J Pathol*, 2003. 163(6): p. 2513–22. [PubMed: 14633623]
45. Lu JP, Monardo L, Bryskin I, Hou ZF, Trachtenberg J, Wilson BC, et al. . Androgens induce oxidative stress and radiation resistance in prostate cancer cells through NADPH oxidase. *Prostate Cancer Prostatic Dis*, 2010. 13(1): p. 39–46. [PubMed: 19546883]
46. Pinthus JH, Bryskin I, Trachtenberg J, Lu JP, Singh G, Fridman E, et al. . Androgen induces adaptation to oxidative stress in prostate cancer: implications for treatment with radiation therapy. *Neoplasia*, 2007. 9(1): p. 68–80. [PubMed: 17325745]
47. Marcias G, Erdmann E, Lapouge G, Siebert C, Barthélémy P, Duclos B, et al. . Identification of novel truncated androgen receptor (AR) mutants including unreported pre-mRNA splicing variants in the 22Rv1 hormone-refractory prostate cancer (PCa) cell line. *Hum Mutat*, 2010. 31(1): p. 74–80. [PubMed: 19830810]
48. White MA, Lin C, Rajapakshe K, Dong J, Shi Y, Tsouko E, et al. . Glutamine Transporters Are Targets of Multiple Oncogenic Signaling Pathways in Prostate Cancer. *Mol Cancer Res*, 2017. 15(8): p. 1017–1028. [PubMed: 28507054]

49. Xu L, Yin Y, Li Y, Chen X, Chang Y, Zhang H, et al. , A glutaminase isoform switch drives therapeutic resistance and disease progression of prostate cancer. *Proc Natl Acad Sci U S A*, 2021. 118(13).
50. Galan-Cobo A, Sitthideatphaiboon P, Qu X, Poteete A, Pisegna MA, Tong P, et al. , LKB1 and KEAP1/NRF2 Pathways Cooperatively Promote Metabolic Reprogramming with Enhanced Glutamine Dependence in KRAS-Mutant Lung Adenocarcinoma. *Cancer Res*, 2019. 79(13): p. 3251–3267. [PubMed: 31040157]
51. Gross MI, Demo SD, Dennison JB, Chen L, Chernov-Rogan T, Goyal B, et al. , Antitumor activity of the glutaminase inhibitor CB-839 in triple-negative breast cancer. *Mol Cancer Ther*, 2014. 13(4): p. 890–901. [PubMed: 24523301]
52. McBrayer SK, Mayers JR, DiNatale GJ, Shi DD, Khanal J, Chakraborty AA, et al. , Transaminase Inhibition by 2-Hydroxyglutarate Impairs Glutamate Biosynthesis and Redox Homeostasis in Glioma. *Cell*, 2018. 175(1): p. 101–116.e25. [PubMed: 30220459]
53. Myint ZW, Sun RC, Hensley PJ, James AC, Wang P, Strup SE, et al. , Evaluation of Glutaminase Expression in Prostate Adenocarcinoma and Correlation with Clinicopathologic Parameters. *Cancers (Basel)*, 2021. 13(9).
54. Kirshner JR, He S, Balasubramanyam V, Kepros J, Yang CY, Zhang M, et al. , Elesclomol induces cancer cell apoptosis through oxidative stress. *Mol Cancer Ther*, 2008. 7(8): p. 2319–27. [PubMed: 18723479]
55. O'Day S, Gonzalez R, Lawson D, Weber R, Hutchins L, Anderson C, et al. , Phase II, randomized, controlled, double-blinded trial of weekly elesclomol plus paclitaxel versus paclitaxel alone for stage IV metastatic melanoma. *J Clin Oncol*, 2009. 27(32): p. 5452–8. [PubMed: 19826135]
56. Reitzer LJ, Wice BM, and Kennell D, Evidence that glutamine, not sugar, is the major energy source for cultured HeLa cells. *J Biol Chem*, 1979. 254(8): p. 2669–76. [PubMed: 429309]
57. Wagner A, Marc A, Engasser JM, and Einsele A, Growth and metabolism of human tumor kidney cells on galactose and glucose. *Cytotechnology*, 1991. 7(1): p. 7–13. [PubMed: 22359153]
58. Arroyo JD, Jourdain AA, Calvo SE, Ballarano CA, Doench JG, Root DE, et al. , A Genome-wide CRISPR Death Screen Identifies Genes Essential for Oxidative Phosphorylation. *Cell Metab*, 2016. 24(6): p. 875–885. [PubMed: 27667664]
59. Sheftel AD, Stehling O, Pierik AJ, Elsässer HP, Mühlenhoff U, Webert H, et al. , Humans possess two mitochondrial ferredoxins, Fdx1 and Fdx2, with distinct roles in steroidogenesis, heme, and Fe/S cluster biosynthesis. *Proc Natl Acad Sci U S A*, 2010. 107(26): p. 11775–80. [PubMed: 20547883]
60. Shi Y, Ghosh M, Kovtunovych G, Crooks DR, and Rouault TA, Both human ferredoxins 1 and 2 and ferredoxin reductase are important for iron-sulfur cluster biogenesis. *Biochim Biophys Acta*, 2012. 1823(2): p. 484–92. [PubMed: 22101253]
61. Wikvall K, Hydroxylations in biosynthesis of bile acids. Isolation of a cytochrome P-450 from rabbit liver mitochondria catalyzing 26-hydroxylation of C27-steroids. *J Biol Chem*, 1984. 259(6): p. 3800–4. [PubMed: 6423637]
62. Yoon PS, Rawlings J, Orme-Johnson WH, and DeLuca HF, Renal mitochondrial ferredoxin active in 25-hydroxyvitamin D3 1 alpha-hydroxylase. Characterization of the iron-sulfur cluster using interprotein cluster transfer and electron paramagnetic resonance spectroscopy. *Biochemistry*, 1980. 19(10): p. 2172–6. [PubMed: 6246922]
63. Chu J-W and Kimura T, Studies on Adrenal Steroid Hydroxylases: COMPLEX FORMATION OF THE HYDROXYLASE COMPONENTS. *Journal of Biological Chemistry*, 1973. 248(14): p. 5183–5187. [PubMed: 4146190]
64. Hwang PM, Bunz F, Yu J, Rago C, Chan TA, Murphy MP, et al. , Ferredoxin reductase affects p53-dependent, 5-fluorouracil-induced apoptosis in colorectal cancer cells. *Nat Med*, 2001. 7(10): p. 1111–7. [PubMed: 11590433]
65. Liu G and Chen X, The ferredoxin reductase gene is regulated by the p53 family and sensitizes cells to oxidative stress-induced apoptosis. *Oncogene*, 2002. 21(47): p. 7195–204. [PubMed: 12370809]
66. Mitani F and Ichiyama A, Enzymic studies on adrenocortical deoxycorticosterone 11beta-hydroxylase system. *J Biol Chem*, 1975. 250(20): p. 8010–5. [PubMed: 1176457]



process for the treatment, digestion, and analysis of patient-derived PCa explants. **(O)** ROS assays of patient-derived explants shows the effect of treatment with V or 10 μ M E for 48 hrs *ex vivo* (n = 3, Unpaired t-test). Statistical significance: *P < 0.05, **P < 0.01, ***P < 0.001, data represents mean or median +/- SEM.

Author Manuscript

Author Manuscript

Author Manuscript

Author Manuscript

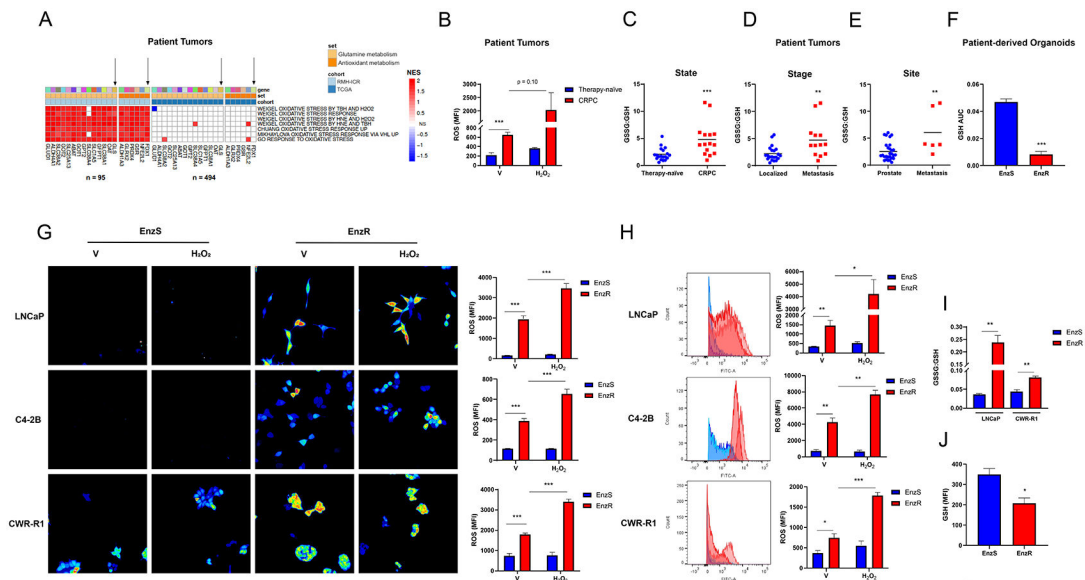


Figure 2. EnzR cells and antiandrogen-treated CRPC tumors have increased basal and inducible ROS:

(A) Heatmap shows the pathway enrichment analysis and GSEA normalized enrichment scores correlating glutamine and antioxidant metabolism genes and oxidative stress pathways from therapy-naïve patient tumors from the TCGA cohort ($n = 494$) and enzalutamide and abiraterone-treated CRPC patient tumors from the RMH-ICR cohort ($n = 95$, Multiple t-tests). (B) ROS assays of PCa patient tumors show the effect of treatment with vehicle (V) or 1 mM H_2O_2 for 15 mins in suspension (therapy-naïve: $n = 6$, CRPC: $n = 5$, Paired t-test (for treatment comparison) and Unpaired t-test (for basal comparison)). (C) GSSG:GSH from steady-state metabolomics of therapy-naïve ($n = 19$) and CRPC ($n = 15$, Mann-Whitney U test) PCa patient tumors are shown and correlated with disease state (D) metastasis status (stage) and (E) tumor site. (F) Steady-state metabolomics shows GSH levels in EnzS LNCaP organoids ($n = 6$) and 3 EnzR patient-derived organoids ($n = 18$, VIP score). (G) ROS assays of EnzS/EnzR cells shows the effect of treatment with V or 1 mM H_2O_2 for 30 mins and assessment by fluorescence microscopy ($n = 3$ per EnzS/EnzR pair, Unpaired t-test) or (H) flow cytometry (LNCaP: $n = 5$, C4-2B $n = 3$, CWR-R1: $n = 5$, Unpaired t-test). (I) Quantitative GSSG:GSH assays performed by steady-state metabolomics of EnzS/EnzR cells show the basal differences in GSSG:GSH ($n = 3$, Unpaired t-test). (J) GSH assay of EnzS/EnzR LNCaP cells by flow cytometry show basal differences in GSH levels ($n = 3$, Unpaired t-test). Metabolites extracted in 80% MeOH + 0.1% formic acid. Statistical significance: * $P < 0.05$, ** $P < 0.01$, *** $P < 0.001$; *VIP score > 1.0 , **VIP score > 1.1 , ***VIP score > 1.2 , data represents mean or median \pm SEM.

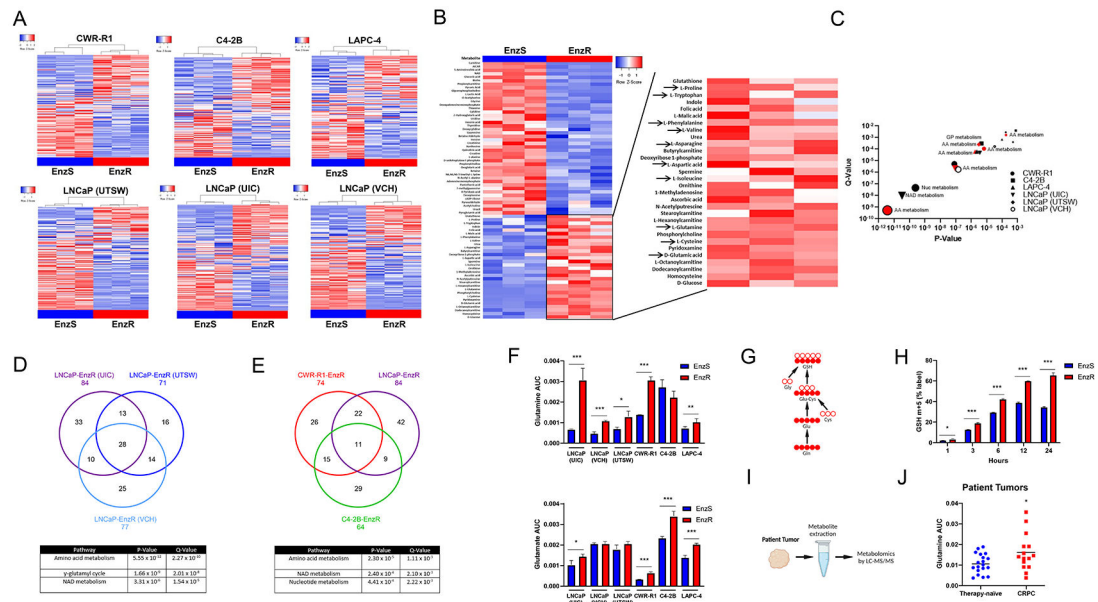


Figure 3. EnzR cells and CRPC tumors have enhanced glutamine metabolism: (A) Heatmaps depict steady-state metabolomics of EnzS/EnzR cells (n = 3). (B) Heatmap of steady-state metabolomics show significantly altered metabolites (FC > 2) in EnzS/EnzR CWR-R1 cells (n = 3, VIP score). (C) Representation of steady-state metabolomics illustrates significantly over-represented pathways by p-value and q-value from pathway analysis of significantly altered metabolites in EnzS/EnzR cells (n = 3, VIP score). (D-E) Venn diagrams and over-representation pathway analysis show significantly altered metabolites by steady-state metabolomics in EnzS/EnzR cells (n = 3, VIP score). (F) Steady-state metabolomics show the glutamine and glutamate levels in EnzS/EnzR cells (n = 3, VIP score). (G) Diagram shows the flux of metabolites assessed by ^{13}C -glutamine isotope tracing. (H) ^{13}C -glutamine isotope tracing shows the glutamine flux to GSH in EnzS/EnzR LNCaP cells (n = 3, Unpaired t-test). (I) Flow diagram shows the process for performing metabolomics of patient PCa tumors. (J) Steady-state metabolomics shows the glutamine levels in therapy-naïve (n = 19) and CRPC (n = 15, Unpaired t-test) PCa patient tumors. Statistical significance: *P < 0.05, **P < 0.01, ***P < 0.001; *VIP score > 1.0, **VIP score > 1.1, ***VIP score > 1.2, data represents mean +/- STD.

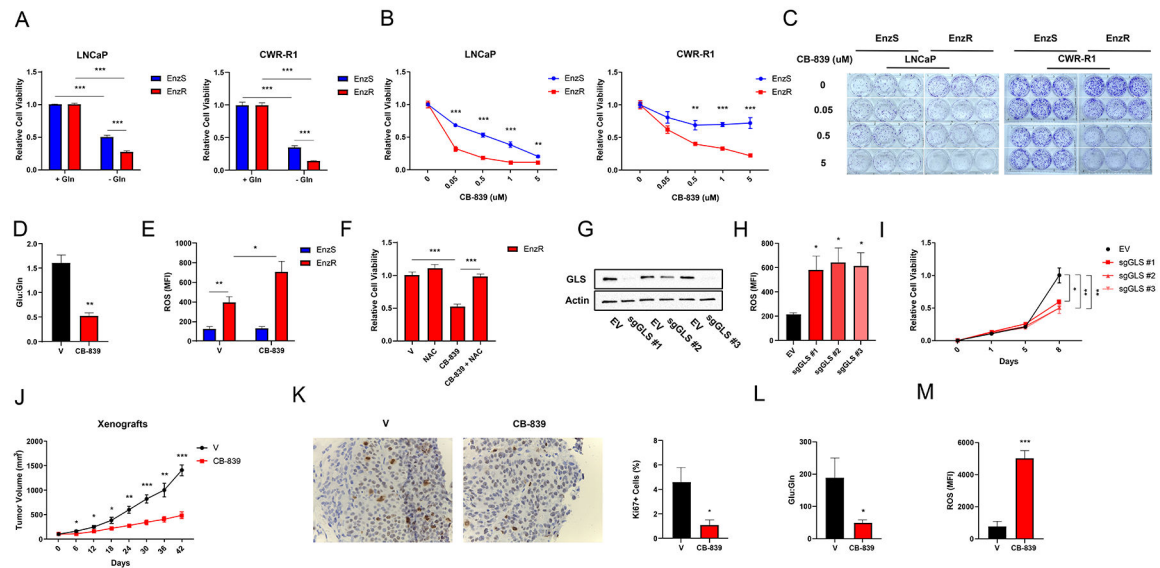


Figure 4. EnzR cells are vulnerable to glutamine blockade:

(A) Cell viability assays show the viability of EnzS/EnzR cells in the presence and absence of glutamine (Gln) after 7 days (LNCaP: n = 4, CWR-R1: n = 8, Unpaired t-test). (B) Cell viability assays show the viability of EnzS/EnzR cells treated with vehicle (V) or CB-839 for 7 days (LNCaP: n = 4, CWR-R1: n = 4, Unpaired t-test). (C) Colony formation assays show the colonies of EnzS/EnzR cells treated with V or CB-839 for 14 days (n = 3 for each EnzS/EnzR pair). (D) Steady-state metabolomics show the glutamate (Glu): glutamine (Gln) ratio in LNCaP-EnzR cells treated with V or 1 μ M CB-839 for 24 hrs (n = 3, Unpaired t-test). (E) ROS assays show the ROS levels of EnzS/EnzR LNCaP cells treated with V or 500 nM CB-839 for 3 days (n = 4, Unpaired t-test). (F) Cell viability assays show the viability of LNCaP-EnzR cells treated with V, 1 mM N-acetylcysteine (NAC), 50 nM CB-839, or CB-839 + NAC for 7 days (n = 4, Unpaired t-test). (G) Western blot shows the GLS levels of CWR-R1-EnzR cells with empty vector (EV) or GLS-targeted guides (n = 3). (H) ROS assays show the ROS levels of CWR-R1-EnzR cells with EV or GLS-targeted guides (n = 3, Unpaired t-test). (I) Cell viability assays show the growth of CWR-R1-EnzR cells with EV or GLS-targeted guides (n = 4, Unpaired t-test). (J) Tumor growth curve shows the growth of CWR-R1-EnzR mouse xenografts treated with V or 200 mg/kg CB-839 for 42 days (V: n = 8, CB-839: n = 7, Multiple t-tests). (K) IHC and quantification shows Ki67 staining of CWR-R1-EnzR mouse xenografts treated with V or CB-839 under the same conditions (V: n = 5, CB-839: n = 6, Unpaired t-test). (L) Steady-state metabolomics shows the Glu:Gln ratio of mouse xenograft tumors treated with V or CB-839 under the same conditions, normalized to plasma concentrations (V: n = 5, CB-839: n = 6, Unpaired t-test). (M) ROS assays show the ROS levels of mouse xenograft tumors treated with V or CB-839 under the same conditions (V: n = 4, CB-839: n = 6, Unpaired t-test). Statistical significance: *P < 0.05, **P < 0.01, ***P < 0.001, data represents mean or median \pm SEM.

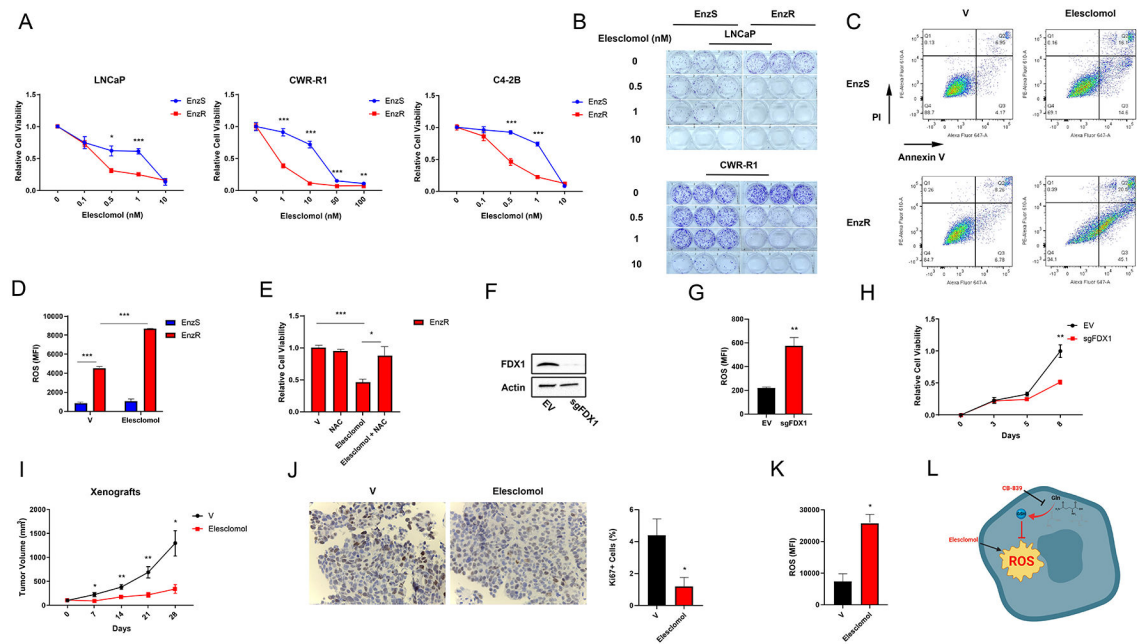


Figure 5. EnzR cells are vulnerable to ferredoxin blockade:

(A) Cell viability assays show the viability of EnzS/EnzR cells treated with vehicle (V) or elesclomol for 7 days (n = 4, Unpaired t-test). (B) Colony formation assays show the colonies of EnzS/EnzR cells treated with V or elesclomol for 14 days (n = 3). (C) Apoptosis assays by Annexin V and propidium iodide (PI) staining shows the percentage of cells with early (Q3) and late apoptosis (Q2) in EnzS/EnzR C4-2B cells treated with V or 10 nM elesclomol for 3 days (n = 3, Unpaired t-test). (D) ROS assays show the ROS levels of EnzS/EnzR C4-2B cells treated with V or 10 nM elesclomol for 3 days (n = 3, Unpaired t-test). (E) Cell viability assays show the viability of LNCaP-EnzR cells treated with V, 1 mM N-acetylcysteine (NAC), 350 pM elesclomol, or elesclomol + NAC for 7 days (n = 3, Unpaired t-test). (F) Western blot shows the levels of FDX1 in CWR-R1-EnzR cells with empty vector (EV) or sgFDX1 (n = 3). (G) ROS assays show the ROS levels of CWR-R1-EnzR cells with EV or sgFDX1 (n = 3, Unpaired t-test). (H) Cell viability assays show the growth of CWR-R1-EnzR cells with EV or sgFDX1 (n = 4, Unpaired t-test). (I) Tumor growth curve shows the growth of CWR-R1-EnzR mouse xenografts treated with vehicle or 40 mg/kg elesclomol for 28 days (n = 4 per group, Multiple t-tests). (J) IHC and quantification shows the Ki67 staining of mouse xenografts treated with V or elesclomol under the same conditions (V: n = 3, Elesclomol: n = 4, Unpaired t-test). (K) ROS assays show the ROS levels of mouse xenograft tumors treated with V or elesclomol under the same conditions (V: n = 4, Elesclomol: n = 3, Unpaired t-test). (L) Diagram depicts the molecular changes in EnzR-PCa and the vulnerabilities that can be therapeutically targeted. Statistical significance: *P < 0.05, **P < 0.01, ***P < 0.001, data represents mean or median +/- SEM.

Table 1.
Patient information for patient-derived tumors treated with enzalutamide *ex vivo*:

Therapy-naïve PCa patient tissue information, including gleason score (GS), for patient-derived explants treated *ex vivo* and assessed by ROS assay.

Patient Number	GS
1	7
2	9
3	7

Author Manuscript

Author Manuscript

Author Manuscript

Author Manuscript

Table 2.
Patient informative for therapy-naïve and CRPC tumors assessed by ROS assay:

Therapy-naïve and CRPC PCa patient tissue information, including tissue type, therapy, gleason score (GS), tumor source, and metastatic site for tumors assessed by ROS assay. Therapies include radiation (RT), androgen deprivation therapy (ADT), AR-targeted therapies: bicalutamide (Bic), enzalutamide (Enz), abiraterone (Abi), chemotherapy: cabitaxel (Cab), unspecified chemotherapy (Chemo).

Patient Number	Tissue Type	Therapy	GS	Tumor Source	Metastatic Site
1	Therapy-naïve	Naïve	7	Prostate	N/A
2	Therapy-naïve	Naïve	8	Prostate	N/A
3	Therapy-naïve	Naïve	9	Prostate	N/A
4	Therapy-naïve	Naïve	8	Prostate	N/A
5	Therapy-naïve	Naïve	7	Prostate	N/A
6	Therapy-naïve	Naïve	9	Prostate	N/A
1	CRPC	ADT, Abi, Enz, Caba	10	Prostate	Bone (widespread metastasis)
2	CRPC	ADT, Abi, Chemo	N/A	Prostate	N/A
3	CRPC	RT, ADT	8	Prostate	N/A
4	CRPC	ADT, Bic	8	Prostate	N/A
5	CRPC	N/A	10	Prostate	N/A

Table 3.
Patient information for therapy-naïve and CRPC tumors assessed by metabolomics:

Therapy-naïve and CRPC PCa patient tissue information, including tissue type, therapy, gleason score (GS), tumor source, and metastatic site, for cohort assessed by metabolomics. Therapies include radiation (RT), androgen deprivation therapy (ADT), AR-targeted therapies: bicalutamide (Bic), apalutamide (Apa), enzalutamide (Enz), abiraterone (Abi), darolutamide (Daro), chemotherapy: cabazitaxel (Caba), docetaxel (Doce). Tumor sources include prostate and metastasis (Met).

Patient Number	Tissue Type	Therapy	GS	Tumor Source	Metastatic Site
1	Therapy-naïve	Naïve	9	N/A	N/A
2	Therapy-naïve	Naïve	7	N/A	N/A
3	Therapy-naïve	Naïve	8	N/A	N/A
4	Therapy-naïve	Naïve	9	N/A	N/A
5	Therapy-naïve	Naïve	7	N/A	N/A
6	Therapy-naïve	Naïve	8	N/A	N/A
7	Therapy-naïve	Naïve	8	N/A	N/A
8	Therapy-naïve	Naïve	8	N/A	N/A
9	Therapy-naïve	Naïve	7	N/A	N/A
10	Therapy-naïve	Naïve	7	N/A	N/A
11	Therapy-naïve	Naïve	7	N/A	N/A
12	Therapy-naïve	Naïve	8	N/A	N/A
13	Therapy-naïve	Naïve	9	N/A	N/A
14	Therapy-naïve	Naïve	7	N/A	N/A
15	Therapy-naïve	Naïve	7	N/A	N/A
16	Therapy-naïve	Naïve	7	N/A	N/A
17	Therapy-naïve	Naïve	7	N/A	N/A
18	Therapy-naïve	Naïve	N/A	N/A	N/A
19	Therapy-naïve	Naïve 0	9	N/A	N/A
1	CRPC	RT, ADT Bic, Apa, Doce	9	Met	Bone
2	CRPC	RT, ADT, Bic, Enz	8	Prostate	Bone
3	CRPC	RT, ADT, Bic	9	Prostate	Bone
4	CRPC	ADT, Abi, Enz, Olaparib Zometa	N/A	Prostate	Bone and soft tissue
5	CRPC	ADT, Daro	9	Prostate	Bone
6	CRPC	ADT, Abi, Enz, Caba	10	Prostate	Bone (widespread metastasis)
7	CRPC	ADT, Abi, Bic, Enz	9	Prostate	Bone
8	CRPC	ADT, Apa	9	Prostate	Bone
9	CRPC	RT, ADT	8	Prostate	N/A
10	CRPC	ADT, Daro	7	Prostate	N/A
11	CRPC	ADT, RT, Bic, Enz	8	Met	Bone
12	CRPC	RT, ADT, Abi, Apa, Xofigo, Doce	9	Met	Bone (Femur)

Patient Number	Tissue Type	Therapy	GS	Tumor Source	Metastatic Site
13	CRPC	ADT, Bic, Enz	10	Met	Pelvis (connective and soft tissue)
14	CRPC	RT, ADT, ADT, Abi, Doce	9	Met	Seminal vesicle
15	CRPC	RT, ADT, Bic	8	Met	Bladder

Author Manuscript

Author Manuscript

Author Manuscript

Author Manuscript